A Fast ISAR Tomography Technique for Fully Polarimetric 3-D Imaging of Man-Made Targets

Kejiang Wu and Xiaojian Xu

Abstract—**The 3-D inverse synthetic aperture radar (ISAR) tomography is an enabling technique for applications such as the exact diagnosis of scattering mechanisms for complex targets. Nevertheless, current ISAR tomography solutions still suffer from problems such as the great computational complexity and optimal utilization of the signatures acquired from limited baselines. In this work, we propose a fast ISAR tomography technique for fully polarimetric 3-D imaging of man-made targets. A stack of 2-D complex-valued images with different baselines and polarizations is first obtained through a phase error calibration (PEC) process and graphic processing unit accelerated polarimetric filtered backprojection. A polarimetric state-space decomposition (P-SSD) algorithm is then developed which could provide joint 3-D reconstruction results with low computational complexity. Examples from both numerical multibaseline data for the Sandia laboratories implementation of cylinders (SLICY) benchmark model and the outdoor range dataset collected by the Georgia Tech Research Institute (GTRI) are presented to demonstrate the superior performance and the usefulness of the proposed technique.**

Index Terms—**Fully polarimetric 3-D imaging, inverse synthetic aperture radar (ISAR) tomography, polarimetric state-space decomposition (P-SSD).**

I. Introduction

In recent years, there is an increasing concern in 3-D synthetic aperture radar (SAR) or inverse SAR (ISAR) imaging [1]–[4], which is considered to be an extension of the traditional 2-D SAR or ISAR imaging techniques. By using 3-D imagery, scattering mechanisms on a complex radar target can be clearly presented and studied in 3-D space for further applications, such as exact scattering diagnosis and automatic target recognition [5], [6]. In this way, problems in 2-D SAR/ISAR images could be fundamentally overcome [7].

To achieve 3-D high-resolution imagery of radar targets, different techniques, i.e., interferometric SAR/ISAR and multibaseline tomography, have been developed [8], [9]. The classical interferometric SAR/ISAR exploits the phase differences between two 2-D radar images to derive the altitude information of the target. However, interferometry does not enable resolving among multiple scattering centers in the same down and cross range resolution cells in elevation [10]. This problem has motivated the development of tomographic SAR/ISAR that utilizes the coherence of 2-D complex-valued images acquired from multiple baselines.

Typically, the formation of 3-D high-resolution images using Fourier-based tomography requires the number of baseline collections, which results in a much greater burden on both data acquisition and processing. In order to improve the elevation resolution with limited baseline collections, a variety of super-resolution (SR) techniques has been developed for the tomographic height/elevation inversion of target scattering centers [11]–[18].

For instance, in [13]–[16], investigations of the spectral estimation techniques, which include the multilook relaxation (M-RELAX), the multilook amplitude and phase estimation (M-APES), the multiple signal classification (MUSIC), and the Capon algorithms, have been made for the tomographic elevation inversion process. The experimental results and the Cramer–Rao lower bounds calculation demonstrate the SR ability in the elevation direction. Apart from the aforementioned spectral estimation techniques, another important kind is the algorithm based on compressed sensing (CS) theory [3], [10]–[12]. In [10], a time-domain CS-based tomography process is proposed, where the basis matrix constructed by a sinc kernel function and basis pursuit denoising technique are applied to the elevation estimation of scattering centers. In [3], [11], [12], and [18], a series of frequency-domain CS-based approaches have been introduced for the spaceborne or airborne SAR tomography, which could achieve significant resolution improvement with sparse baselines. Compared to the spectral estimation techniques, the CS-based techniques have advantages in processing the nonuniform baselines but with a time-consuming iterative process [18]. Furthermore, an overview of the SR-based tomography techniques can be found in [11] and [13].

More recently, the use of SR-based tomography with fully polarimetric data has been investigated in [5] and [7]. Compared with the single polarization case, the fully polarimetric tomography can not only provide 3-D scattering features of targets but also the polarimetric information of each scattering center [17]. However, there are still several issues that restrict the practical use of SR-based fully polarimetric tomography. First, since all the 2-D images of each baseline and all the down range-cross range resolution cells are required to process independently, the computational complexity of each processing step should be considered especially for the fully polarimetric large-scale practice [18]–[20]. Second, as a joint processing framework to the fully polarimetric

Manuscript received April 20, 2021; revised June 11, 2021; accepted July 8, 2021. Date of publication July 29, 2021; date of current version January 14, 2022. *(Corresponding author: Xiaojian Xu.)*

The authors are with the School of Electronic and Information Engineering, Beihang University, Beijing 100191, China (e-mail: wukejiang88@buaa.edu.cn; xiaojianxu@buaa.edu.cn).

Digital Object Identifier 10.1109/TGRS.2021.3097725

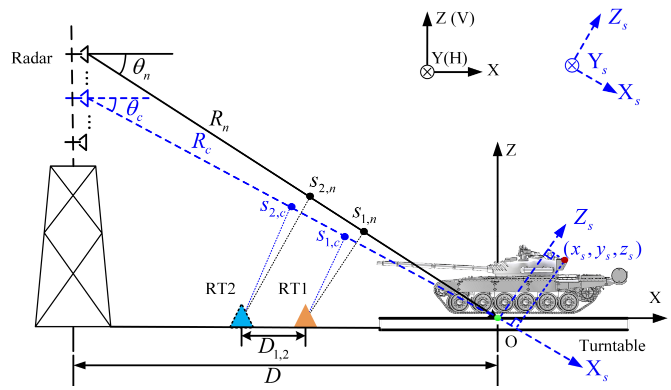

Fig. 1. Geometry of the ISAR tomography system.

and multibaseline data, it suffers from the errors caused by outdoor measurements, zero-Doppler clutter (ZDC), and the uncertainty of parameter estimation [3], [7], [21]–[23].

In this article, we focus on developing a new ISAR tomography technique for fully polarimetric 3-D imaging of man-made targets. In general, the main contributions of this article are given as follows. First, a novel 3-D ISAR tomography framework based on the polarimetric state-space decomposition (P-SSD) is proposed, which has superior computational efficiency, SR capability, and fully polarimetric imagery. Second, a frequency-domain phase error calibration (PEC) process is applied to eliminate the phase error caused by outdoor measurements. Finally, the performance of the proposed technique has been validated using both numerical and outdoor range datasets. The results show that the proposed technique is useful for 3-D tomographic reconstruction of the real-world complex targets with limited baseline collections.

The remainder of the article is organized as follows. A brief review of the signal model for ISAR tomography is first made in Section II. Detailed mathematics and procedure for the proposed framework are discussed in Section III. In Section IV, 3-D tomographic image examples are presented, where both numerical multibaseline data for the Sandia laboratories implementation of cylinders (SLICY) benchmark model [24] and the outdoor range dataset collected by the Georgia Tech Research Institute (GTRI) [25] are used. The performances of different elevation inversion techniques are compared to demonstrate the usefulness of the currently proposed technique. We conclude the article in Section V.

II. Signal Model

The geometry of the 3-D ISAR tomography (TomoISAR) system is shown in Fig. 1. As can be seen, the target is placed on a turntable and observed with a monostatic radar. The monostatic radar is placed on an elevator platform, and thus, the height of the antenna can be manually changed [26]. Consequently, the multibaseline data can be obtained by repeating the ISAR measurement with different elevation angles.

As previously stated, a whole TomoISAR procedure mainly includes a 2-D imaging process followed by the parameter estimation of the elevation direction. We first consider the problem of 2-D ISAR imaging at the slant-range plane ($X_s O Y_s$ plane in Fig. 1). As a 2-D projection of the 3-D scattering distribution function, the scattering function [8] in the 2-D imaging plane can be expressed as

$$\begin{aligned}\mathbf{I}_{\text{pol}}(x_s, y_s, \theta_n) = &\iint_{f,\varphi} \sigma_{\text{pol}}(f, \varphi, \theta_n)\\ &\cdot \exp\left[-j\frac{4\pi f}{c}R(x_s, y_s, \varphi, \theta_n)\right] df\, d\varphi \qquad (1)\end{aligned}$$

where f is the step frequency, φ is the azimuth angle, and $\theta_n = \theta_0 + n\Delta\theta$ is the elevation angle. $\sigma_{\text{pol}}(f, \varphi, \theta_n)$ represents the radar signature acquired from different frequencies and azimuth angles in the same elevation angle, $R(x_s, y_s, \varphi, \theta_n)$ is the distance between radar antennas and target, and (x_s, y_s) denotes the coordinate of the target in the slant-range plane.

Typically, each resolution cell of the 2-D image sequences $\{\mathbf{I}_{\text{pol}}(x_s, y_s, \theta_n)\}_{n=1}^{N}$ obtained from (1) can be accurately approximated by using the undamped scattering center model [3], [7], [18]. Considering that different scattering geometries usually have different angle dependences [27]–[29], we select the damped exponential (DE) model to be the parametric model of the elevation direction. The adopted DE model is based on the geometrical theory of diffraction (GTD) and derived from the attributed scattering center (ASC) model [28]. As described in [29] and [43], if multiple transmit–receive polarization pairs are available, the scattering centers of different polarizations share the same angle dependence but with different amplitudes

$$\begin{aligned}\mathbf{I}_{\text{pol}}(x_s, y_s, \theta_n) = &\sum_{k=1}^{K} \alpha_{k,\text{pol}}(x_s, y_s) \exp\left(-\beta_k\theta_n - \frac{j4\pi f_c}{c}\theta_n z_{k,s}\right)\\ &+ w_{\text{pol}} \qquad (2)\end{aligned}$$

where the parameter set $\{\alpha_{k,\text{pol}}(x_s, y_s), \beta_k, z_{k,s}\}$ characterizes these K discrete scattering centers, i.e., $\alpha_{k,\text{pol}}(x_s, y_s)$ represents the complex amplitude, β_k is the angle dependence parameter, and $z_{k,s}$ denotes the relative height of scattering center in the $X_s Y_s Z_s$ coordinate system (see Fig. 1). f_c represents the center frequency, c is the propagation speed of the electromagnetic signal, and w_{pol} stands for the noise.

III. Model-Based ISAR Tomography Technique

The proposed model-based ISAR tomography technique mainly includes the following three processing steps, i.e., PEC, multibaseline 2-D imaging, and elevation inversion. Details are as follows.

A. Phase Error Calibration

The basic premise on which TomoISAR relies is that the same scattering centers in the 2-D images obtained from different baselines can appear in the same resolution cell [21], [22]. To satisfy this requirement, a PEC process is needed to eliminate the phase error caused by the measurement. In [7], the influence of the platform disturbance is considered and an image-domain-based PEC algorithm is presented. In [9], the phase sensitivity in the airborne HoloSAR is studied, and the reference-target (RT) setups are demonstrated to be useful for the PEC procedure. In this section, a PEC algorithm from the frequency domain is introduced for the case of TomoISAR imaging.

The basic idea of the proposed PEC algorithm is to compensate for the phase differences between the selected primary baseline data and the rest. To this end, a reference center and primary baseline should be specified previously. Generally, they are chosen to be the turntable center and the intermediate baseline data $\sigma(f, \varphi, \theta_c = \theta_{N/2})$. Thus, the phase error of the nth baseline can be compensated by

$$\sigma_{ca}(f, \varphi, \theta_n) = \sigma(f, \varphi, \theta_n) \cdot \exp\left\{\frac{j4\pi f}{c}(R_n - R_c)\right\} \quad (3)$$

where $\sigma(f, \varphi, \theta_n)$ denotes the radar signatures obtained from the nth baseline, the parameter f is the frequency, and φ and θ denote the target azimuth angle and the elevation angle. R_n denotes the distance from the antenna phase center of the nth baseline to the reference center, and R_c is the distance from the primary baseline to the reference center

$$R_n = D/\cos\theta_n. \quad (4)$$

Note that (3) gives accurate calibration results when parameters $\{D, \theta_n\}$ are measured accurately. In the case of the platform perturbations or measurement error in practical use, the phase error of the nth baseline needs to be further compensated by using the RTs (fixed strong scattering geometries in imaging area) [9]

$$\sigma_{ca}(f, \varphi, \theta_n) = \sigma(f, \varphi, \theta_n) \cdot \exp\left\{\frac{j4\pi f}{c}\left(R'_n - R''_c + \Delta R_n\right)\right\} \quad (5)$$

where R'_n is the measurement result and ΔR_n represents the phase error caused by distance measurement. Let R''_n denote the actual result and δ_D denote the measurement error of D; thus, ΔR_n is given by

$$\begin{aligned}\Delta R_n &= \left(R''_n - R''_c\right) - \left(R'_n - R'_c\right) \\ &= \delta_D(1/\cos\theta_n - 1/\cos\theta_c).\end{aligned} \quad (6)$$

In the practical measurement, the RT is fixed somewhere outside the turntable, and the position of the corresponding scattering center does not change with the turntable rotation. Then, δ_D can be estimated by utilizing this additional information

$$\delta_D \approx \mathbf{s}_{1,n}/\cos\theta_n - \mathbf{s}_{1,c}/\cos\theta_c \quad (7)$$

where $\mathbf{s}_{1,n}$ denotes the position of the RT1 in the corresponding 1-D high-resolution range profile (HRRP), which is obtained by the fast Fourier transform (FFT).

Note that the measurement phase error can be estimated by using (6) and (7) if the influence of the measurement angle error is not considered. To further estimate the measurement angle error δ_{θ_n}, one possible solution is to use more RTs (see Fig. 1) [9]

$$\delta_{\theta_n} \approx \cos^{-1}\left[(\mathbf{s}_{1,n} - \mathbf{s}_{2,n})/D_{1,2}\right] - \theta'_n \quad (8)$$

where $D_{1,2}$ is the distance between these two reference targets and θ'_n is the measurement result.

B. Multibaseline 2-D Imaging

In this section, the calibrated data from each baseline is performed independently by the 2-D imaging process. As described in [9] and [23], there are several efficient 2-D SAR/ISAR imaging algorithms for this purpose, including the polar format algorithm (PFA) [30], the time-domain direct backprojection (DBP) [31], and fast-factorized backprojection (FFBP) [23]. For the parallel implementation consideration, we adopt a graphic processing unit (GPU) accelerated polarimetric filtered backprojection (G-PFBP) algorithm that could be applied to both far-field and near-field conditions. The process mainly consists of the following four steps.

First, the imaging plane should be identified and divided into the $N_x \times N_y$ equispaced grid, which is corresponding to the Cartesian coordinates $\{(x_{k,s}, y_{k,s})\}_{k=1}^{N_x \times N_y}$, where the x-axis represents the cross range direction and the y-axis is the down range direction. Note that the imaging plane is set to be the slant-range plane for the narrow azimuth range case. For the wide azimuth range case (over 180°), it is suggested to be divided into several subapertures and then processed with incoherent addition (for further details, see [9], [31]).

Second, the 1-D HRRP $P_{\varphi,\text{pol}}(l)$ from different azimuth angles and polarizations can be obtained by the FFT process.

Third, the complex amplitude $P_{\varphi,\text{pol}}(L_e)$ is calculated by using the GPU-supported linear interpolation. Moreover, the signatures with different polarizations can share the same integral path. L_e denotes the integral path of each pixel, expressed as

$$L_e = \sqrt{(x_{ra} - x_{k,s})^2 + (y_{ra} - y_{k,s})^2 + (z_{ra})^2} - R_0 \quad (9)$$

where (x_{ra}, y_{ra}, z_{ra}) gives the coordinate of antenna phase center in the slant-range coordinate system ($X_s Y_s Z_s$ in Fig. 1).

Finally, the 2-D image $\mathbf{\Gamma}_{\text{pol}}(x_s, y_s)$ of each polarization is achieved by the integral process of the obtained $P_{\varphi,\text{pol}}(L_e)$ [32]. According to the preset dynamic range threshold T_{dB}, the location of the strong scattering area is then determined by

$$\begin{aligned}\mathbf{I}_{\text{pol}}(x_s, y_s) : \big\{x_s, y_s, &|\mathbf{\Gamma}_{\text{pol}}(x_s, y_s)| \\ &> \max(|\mathbf{\Gamma}_{\text{pol}}(x_s, y_s)|) \cdot 10^{T_{\text{dB}}/20}\big\}.\end{aligned} \quad (10)$$

C. Elevation Inversion

In the previous section, a group of 2-D complex images with multibaseline and multipolarization have been obtained by using the G-PFBP algorithm. A joint parameter estimation technique, which is named P-SSD, is introduced for the elevation inversion process in this section.

In matrix notation, the signatures in (10) can be written as

$$\begin{aligned}\mathbf{G} &= \begin{bmatrix} \mathbf{I}_{\text{HH}}(x_s, y_s) \\ \mathbf{I}_{\text{HV}}(x_s, y_s) \\ \mathbf{I}_{\text{VH}}(x_s, y_s) \\ \mathbf{I}_{\text{VV}}(x_s, y_s) \end{bmatrix} \\ &= \begin{bmatrix} \mathbf{I}_{\text{HH}}(\theta_1) & \mathbf{I}_{\text{HH}}(\theta_2) & \dots & \mathbf{I}_{\text{HH}}(\theta_N) \\ \mathbf{I}_{\text{HV}}(\theta_1) & \mathbf{I}_{\text{HV}}(\theta_2) & \dots & \mathbf{I}_{\text{HV}}(\theta_N) \\ \mathbf{I}_{\text{VH}}(\theta_1) & \mathbf{I}_{\text{VH}}(\theta_2) & \dots & \mathbf{I}_{\text{VH}}(\theta_N) \\ \mathbf{I}_{\text{VV}}(\theta_1) & \mathbf{I}_{\text{VV}}(\theta_2) & \dots & \mathbf{I}_{\text{VV}}(\theta_N) \end{bmatrix}.\end{aligned} \quad (11)$$

Based on the model defined in (2), we set $p_k = \exp(-\beta_k \Delta\theta - j4\pi f_c \Delta\theta z_{k,s}/c)$. Thus, the matrix element $\mathbf{I}_{\text{pol}}(x_s, y_s, \theta_n)$ can be represented as

$$\mathbf{I}_{\text{pol}}(x_s, y_s, \theta_n) = \sum_{k=1}^{K} \tilde{\alpha}_{k,\text{pol}}(x_s, y_s) p_k^n + w_{\text{pol}} \tag{12}$$

where $\tilde{\alpha}_{k,\text{pol}}(x_s, y_s)$ is the corresponding amplitude.

Using (12), the column vector $\mathbf{G}(\theta_n)$ can be decomposed as the matrix form

$$\mathbf{G}(\theta_n) = \mathbf{A}\mathbf{P}^{n-1}\mathbf{T} + \mathbf{W}_n \tag{13}$$

where $\mathbf{W}_n$ is the noise component, and the matrices $\{\mathbf{A}, \mathbf{P}, \mathbf{T}\}$ are

$$\mathbf{A} = \begin{bmatrix} \tilde{\alpha}_{1,\text{HH}} & \tilde{\alpha}_{2,\text{HH}} & \cdots & \tilde{\alpha}_{K,\text{HH}} \\ \tilde{\alpha}_{1,\text{HV}} & \tilde{\alpha}_{2,\text{HV}} & \cdots & \tilde{\alpha}_{K,\text{HV}} \\ \tilde{\alpha}_{1,\text{VH}} & \tilde{\alpha}_{2,\text{VH}} & \cdots & \tilde{\alpha}_{K,\text{VH}} \\ \tilde{\alpha}_{1,\text{VV}} & \tilde{\alpha}_{2,\text{VV}} & \cdots & \tilde{\alpha}_{K,\text{VV}} \end{bmatrix} \mathbf{D} \tag{14}$$

$$\mathbf{P} = \mathbf{D}^{\text{T}} \begin{bmatrix} p_1 & & & \\ & p_2 & & \\ & & \ddots & \\ & & & p_K \end{bmatrix} \mathbf{D} \tag{15}$$

$$\mathbf{T} = \mathbf{D}^{\text{T}} \mathbf{l}_K \tag{16}$$

where the matrix $\mathbf{D}$ represents a $K \times K$ unitary matrix and $\mathbf{l}_K = [1\ 1\ \ldots\ 1]^{\text{T}}$.

As a result, the matrix $\mathbf{G}$ can be rewritten as

$$\mathbf{G} = \left[\mathbf{AT}\ \mathbf{APT}\ \ldots\ \mathbf{AP}^{N-1}\mathbf{T}\right] + \mathbf{W}. \tag{17}$$

As described in [33] and [34], the derived expression in (17) can be solved by the state-space decomposition (SSD) estimator. It should be noted that there are two restrictions when applying the SSD estimator to the elevation inversion process. One is that the requirement of equal interval sampling may not be satisfied in outdoor measurement cases. The current solution is to obtain the equal spaced samples by using the nonuniform FFT [35]. The other one is that the number of scattering centers per resolution cell is limited to the rank of the constructed Hankel matrix $\mathbf{H}_\theta$ [in (18)], whereas the complex targets may have more scattering centers with different heights. To alleviate this problem, more samples $\mathbf{G}(\theta_n)$ can be acquired by using the Burg extrapolation algorithm [36]

$$\mathbf{H}_\theta = \begin{bmatrix} \mathbf{G}_{\text{ext}}(\theta_1) & \mathbf{G}_{\text{ext}}(\theta_2) & \cdots & \mathbf{G}_{\text{ext}}(\theta_L) \\ \mathbf{G}_{\text{ext}}(\theta_2) & \mathbf{G}_{\text{ext}}(\theta_3) & \cdots & \mathbf{G}_{\text{ext}}(\theta_{L+1}) \\ \vdots & \vdots & \vdots & \vdots \\ \mathbf{G}_{\text{ext}}(\theta_{N-L+1}) & \mathbf{G}_{\text{ext}}(\theta_{N-L+2}) & \cdots & \mathbf{G}_{\text{ext}}(\theta_N) \end{bmatrix} \tag{18}$$

where L denotes the length of the sliding window, it is set to be within the interval $[N/2,\ 2N/3]$, and $\mathbf{G}_{\text{ext}}(\theta_n)$ is the extrapolated matrix

$$\mathbf{G}_{\text{ext}}(\theta_n) = \left[\mathbf{G}_{\text{forwardext}}(\theta_n) \quad \mathbf{G}(\theta_n) \quad \mathbf{G}_{\text{backwardext}}(\theta_n)\right] \tag{19}$$

where $\mathbf{G}_{\text{forwardext}}$ and $\mathbf{G}_{\text{backwardext}}$ denote the forward and backward extrapolated signatures by using the Burg algorithm. Typically, the extrapolated sample number is suggested to be within the interval $[0,\ N/2]$.

Then, the singular value decomposition (SVD) technique followed by a model order selection process is used to split the Hankel matrix $\mathbf{H}_\theta$ into the signal and noise component

$$\mathbf{H}_\theta = \mathbf{U}_s \mathbf{R}_s \mathbf{V}_s^* + \mathbf{U}_n \mathbf{R}_n \mathbf{V}_n^* \tag{20}$$

where $\{\mathbf{U}_s,\ \mathbf{R}_s,\ \mathbf{V}_s\}$ belong to the signal component and $\{\mathbf{U}_n,\ \mathbf{R}_n,\ \mathbf{V}_n\}$ belong to the noise component. Alternatively, there are several model order selection criteria that can be used, which are mainly based on the distribution of singular values [33], [37]. Here, we use an eigenvalue sequences' transform criterion that has a relatively low computational complexity [38].

On the basis of the derived expression in (17) and linear systems theory [33], the noiseless Hankel matrix can be further factorized as

$$\tilde{\mathbf{H}} = \begin{bmatrix} \mathbf{A} \\ \mathbf{AP} \\ \vdots \\ \mathbf{AP}^{N-L} \end{bmatrix} \left[\mathbf{T} \quad \mathbf{PT} \quad \ldots \quad \mathbf{P}^L\mathbf{T}\right] = \tilde{\boldsymbol{\Omega}}\tilde{\boldsymbol{\Gamma}} \tag{21}$$

where $\tilde{\boldsymbol{\Omega}} = \mathbf{U}_{sn}(\mathbf{R}_{sn})^{1/2}$ denotes the observability matrix and $\tilde{\boldsymbol{\Gamma}} = (\mathbf{R}_{sn})^{1/2}\mathbf{V}_{sn}^*$ is the controllability matrix.

From (21), it can be derived that

$$\tilde{\boldsymbol{\Omega}}_{-rl}\mathbf{A} = \tilde{\boldsymbol{\Omega}}_{-rf} \tag{22}$$

where $\tilde{\boldsymbol{\Omega}}_{-rl}$ denotes the first $4(N-L)$ rows of the observability matrix and $\tilde{\boldsymbol{\Omega}}_{-rf}$ is the last $4(N-L)$ rows.

Thus, a least-squares solution based on QR decomposition can be found from (22)

$$\mathbf{P} = \mathbf{R}_{-rl}^{-1}\mathbf{Q}_{-rl}^*\tilde{\boldsymbol{\Omega}}_{-rf} \tag{23}$$

where $\mathbf{Q}_{-rl}$ and $\mathbf{R}_{-rl}$ denote the QR matrices of $\tilde{\boldsymbol{\Omega}}_{-rl}$.

In a similar fashion, the matrix $\mathbf{P}$ can also be estimated by

$$\mathbf{P} = \tilde{\boldsymbol{\Gamma}}_{-cf}\mathbf{R}_{-cl}^{-1}\mathbf{Q}_{-cl}^* \tag{24}$$

where $\mathbf{Q}_{-cl}$ and $\mathbf{R}_{-cl}$ are the QR matrices of the first (L-1) columns of the controllability matrix $\tilde{\boldsymbol{\Gamma}}$ and $\tilde{\boldsymbol{\Gamma}}_{-cf}$ is the last $(L-1)$ columns.

According to the derived expression in (15), the parameter vector $\left[p_1\ p_2\ \ldots\ p_K\right]$ can be acquired by the eigenvalue decomposition of $\mathbf{P}$. Consequently, we can construct the Vandermonde matrix

$$\mathbf{S} = \begin{bmatrix} p_1 & p_1^2 & \cdots & p_1^N \\ p_2 & p_2^2 & \cdots & p_2^N \\ \vdots & \vdots & \cdots & \vdots \\ p_K & p_K^2 & \cdots & p_K^N \end{bmatrix}. \tag{25}$$

Thus, the amplitude vector $\mathbf{A}_{\text{pol}} = \left[\tilde{\alpha}_{1,\text{pol}}\ \tilde{\alpha}_{2,\text{pol}}\ \ldots\ \tilde{\alpha}_{K,\text{pol}}\right]$ of each polarization is found by the least-squares solution

$$\begin{bmatrix} \mathbf{A}_{\text{HH}} & \mathbf{A}_{\text{HV}} \\ \mathbf{A}_{\text{VH}} & \mathbf{A}_{\text{VV}} \end{bmatrix} = \begin{bmatrix} \mathbf{I}_{\text{HH}}\mathbf{S}^*(\mathbf{SS}^*)^{-1} & \mathbf{I}_{\text{HV}}\mathbf{S}^*(\mathbf{SS}^*)^{-1} \\ \mathbf{I}_{\text{VH}}\mathbf{S}^*(\mathbf{SS}^*)^{-1} & \mathbf{I}_{\text{VV}}\mathbf{S}^*(\mathbf{SS}^*)^{-1} \end{bmatrix}. \tag{26}$$

From (2) and (12), the height of the scattering center is given by

$$z_{k,s} = \frac{-\arg(p_k)c}{4\pi f_c \Delta\theta}. \tag{27}$$

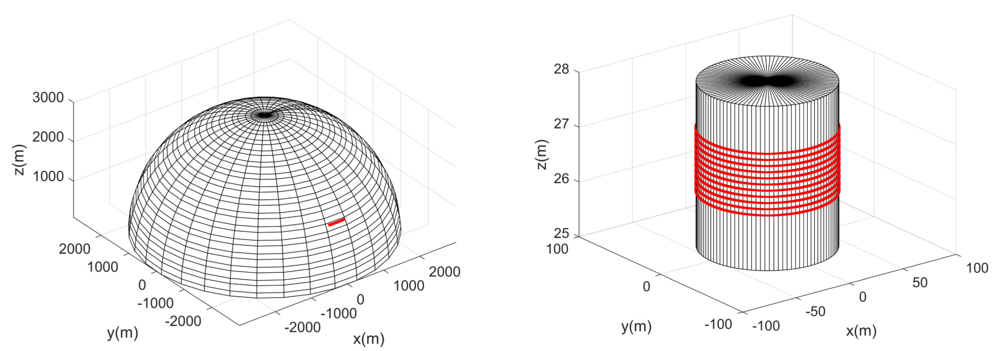

Fig. 2. Radar path of the experimental datasets. (a) Radar path of the numerical dataset collected from the SLICY model. (b) Equivalent radar path of the GTRI dataset. The continuously distributed red points denote the radar positions.

The corresponding parameter of angle dependence is obtained by

$$\beta_k = -\frac{\ln(|p_k|)}{\Delta\theta}. \tag{28}$$

Note that the estimated 3-D scattering points should be rotated back to the horizontal coordinate system since the 2-D imaging plane in Section III-B is set to be the slant-range plane

$$\begin{bmatrix} x_k \\ y_k \\ z_k \end{bmatrix} = \begin{bmatrix} 1 & 0 & 0 \\ 0 & \cos\theta_c & \sin\theta_c \\ 0 & -\sin\theta_c & \cos\theta_c \end{bmatrix} \begin{bmatrix} x_{k,s} \\ y_{k,s} \\ z_{k,s} \end{bmatrix} \tag{29}$$

where θ_c is the elevation angle of the slant-range plane.

IV. Experimental Result

To validate the feasibility of the proposed technique, this section presents some 3-D reconstruction results from both numerical and measurement datasets. The following algorithms, i.e., the superfast line spectral estimation (Superfast LSE) [39] and the polarimetric UMUSIC (P-UMUSIC) [19], are used for comparison. Notice that all the reference algorithms are only applied for the elevation inversion process since all experimental datasets need to be preprocessed by the steps described in Section III-A and III-B.

A. Numerical Data of the SLICY Model

The numerical multibaseline ISAR data are calculated for the Sandia laboratories implementation of cylinders (SLICY) model [6], [24] using the method of shooting and bouncing rays (SBRs). The size of the model in meters is 3.04(length) × 2.7(width) × 1.8(height), and the simulation condition is set as follows. The calculation frequency band is over 9–10 GHz with a frequency step of 10 MHz, full polarization. The target azimuth angle is from -2° to 2° in 0.1° increments, and the elevation angle is from 30° to 29° with an increment of 0.1°.

As can be seen in Fig. 2(a), the simulated radar path is in an ideal sphere with a radius of 3000 m (far-field) so that the phase error is considered to be zero since the distances $\{R_n\}_{n=1}^{11}$ defined in (2) are the same. In the 2-D imaging processing step, the imaging area is divided into a $501(x) \times 501(y)$ uniform rectangle grid, and the imaging plane is set to be the slant-range plane with an elevation angle of 29.5°. The maximum magnitude of the HH polarized 2-D image is used for magnitude normalization, and the strong scattering threshold is $T_{\mathrm{dB}} = 45$. Thus, 11(baseline) × 4 (polarization) 2-D images can be obtained by using the proposed G-PFBP algorithm. Fig. 3 gives 2-D images of the SLICY model using the data of different polarizations (primary baseline). As shown in the figure, the scattering centers of different scattering structures perform significant differences in the amplitudes and shapes. Compared with the copolarization result, there are only several weak scattering centers in the cross-polarization result.

After a joint elevation inversion process to the obtained 44 2-D images, 3-D reconstruction results with different polarizations are shown in Fig. 4. As can be seen in the figure, the reconstructed 3-D scattering points are accurately matched with the SLICY model. For example, there are seven marked strong scattering centers in the HH polarization result. According to the matched result, we can see that the scattering centers 1 and 3 are caused by the scattering of dihedral reflectors, and the scattering centers 4 and 5 are generated by the scattering of the tophat structures. The scattering center 2 is caused by the specular reflection of the cylinder structure, and the scattering center 6 is generated by multiple reflections of the trihedral structure. The scattering center 7 is generated by the combined effect of the odd and even scattering of the drum structure. Table I also lists the locations and polarimetric scattering matrices (PSMs) of the marked seven scattering centers. From the relative phase of the PSM, it can be seen that the marked scattering centers 1, 3, 4, 5, and 6 have phase differences close to 180° in the copolarization components, whereas the scattering center 2 has a phase difference close to 0°. From the relative magnitude of the PSM, we can see that the marked scattering centers 1, 2, 3, 4, 5, and 6 have weak magnitudes in the cross-polarization components, whereas the scattering center 7 has obvious different magnitudes in the cross-polarization components. According to the obtained characteristics of the PSM, we can conclude that the scattering center 6 is caused by an even reflection of the nonstandard trihedral corner reflector, which is in agreement with the ray-tracing result (4-bounce). These results demonstrate that the relative phase differences and magnitudes in copolarization components tend to be a useful feature to distinguish the odd and even scatterings [40], [41]. Besides, it is seen that there are

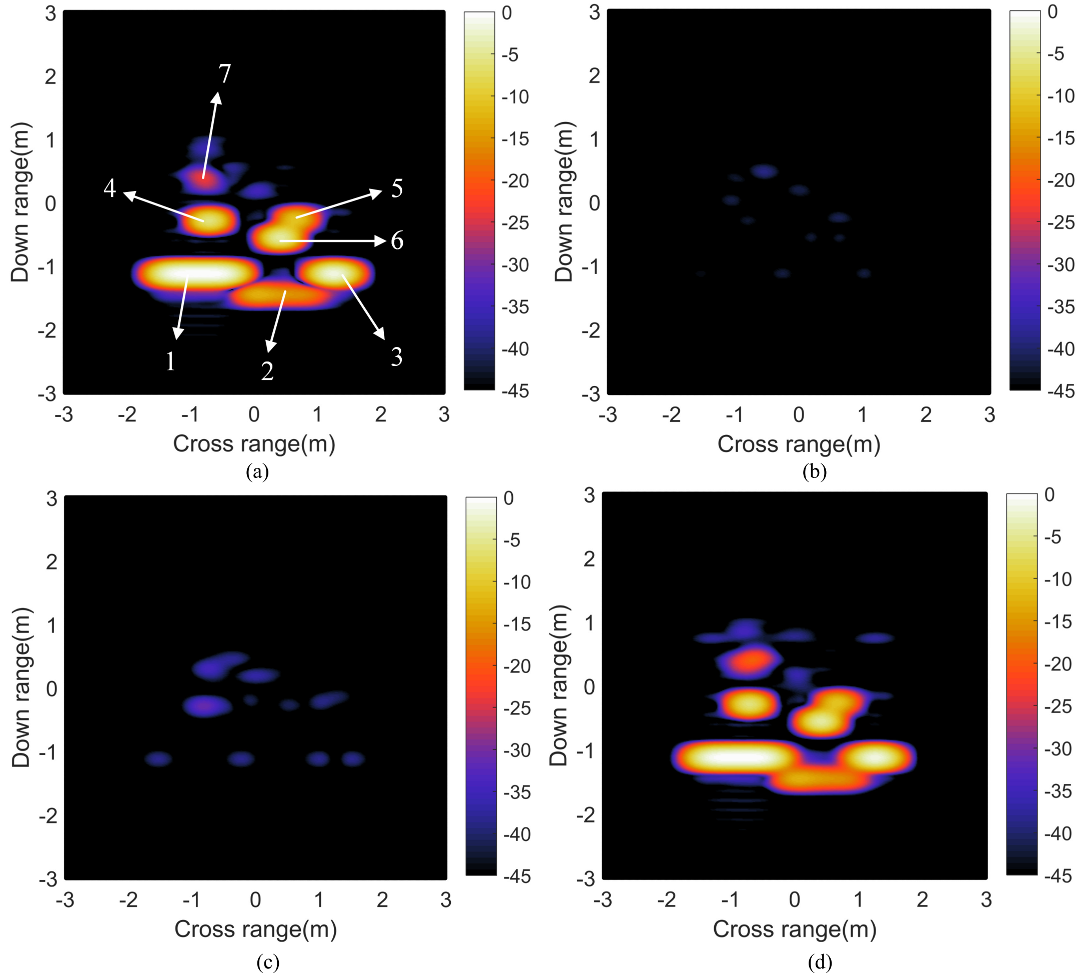

Fig. 3. 2-D image of the SLICY model with different polarizations (primary baseline). (a) HH polarization. (b) HV polarization. (c) VH polarization. (d) VV polarization.

some weak scattering centers spread out of the target surface (the red boxes in Fig. 4). These scattering centers are caused by multireflection of the upside of the SLICY model and can also be observed in the airborne SAR image of the SLICY target [44].

Height estimation errors of the marked scattering centers are given in Table II. The test signatures are added with white Gaussian noise, and the signal-to-noise ratio (SNR) is set to be 30–0 dB (200 Monte Carlo trials for each SNR). The root mean square error (RMSE) [15] is used for evaluating the accuracy. The results show that the proposed P-SSD performs robustly in height estimation for low SNR.

B. Outdoor Measurement Data

The measurement data of a full-size T72 tank are used in the imaging example presented here. These data belong to the moving and stationary target acquisition recognition (MSTAR) dataset and are collected by GTRI [25]. The measurement scenario is the same as that shown in Fig. 1. The radar is placed on the elevator platform of a fixed high tower. The platform has a 1-ton bearing capacity, and its height can be adjusted between 0.91 and 27.43 m. The turntable is 45.72 m away from the launch tower, with a radius of 6.858 meters and a bearing capacity of 100 tons. Large man-made targets (such as T72 tank) can be placed on it. When the radar collects data, the turntable can rotate 1–10 revolutions per hour to form the virtual aperture along the azimuth dimension.

TABLE I

ESTIMATED RESULTS OF THE MARKED SCATTERING CENTERS

Marked number	Locations (X, Y, Z)	Polarimetric scattering matrix
1	(-0.89m, -0.97m, 0.45m)	$0.44e^{j48.3^\circ}\begin{bmatrix} 1 & 0.00e^{j-38.3^\circ} \\ 0.00e^{j-24.8^\circ} & 1.00e^{j-177.2^\circ} \end{bmatrix}$
2	(0.42m, -1.30m, 0.60m)	$0.11e^{j-72.8^\circ}\begin{bmatrix} 1 & 0.00e^{j7.4^\circ} \\ 0.00e^{j45.7^\circ} & 1.00e^{j0.08^\circ} \end{bmatrix}$
3	(1.27m, -0.99m, 0.46m)	$0.38e^{j86.2^\circ}\begin{bmatrix} 1 & 0.00e^{j79.4^\circ} \\ 0.00e^{j97.6^\circ} & 1.00e^{j-176.1^\circ} \end{bmatrix}$
4	(-0.69m, 0.18m, 0.80m)	$0.23e^{j-163.7^\circ}\begin{bmatrix} 1 & 0.01e^{j-28.8^\circ} \\ 0.05e^{j-32.4^\circ} & 1.00e^{j-179.1^\circ} \end{bmatrix}$
5	(0.72m, 0.23m, 0.80m)	$0.13e^{j171.0^\circ}\begin{bmatrix} 1 & 0.03e^{j104.4^\circ} \\ 0.02e^{j71.2^\circ} & 0.99e^{j-177.7^\circ} \end{bmatrix}$
6	(0.42m, -0.21m, 0.80m)	$0.24e^{j-62.0^\circ}\begin{bmatrix} 1 & 0.00e^{j119.3^\circ} \\ 0.00e^{j62.1^\circ} & 1.00e^{j177.1^\circ} \end{bmatrix}$
7	(-0.80m,0.90m,0.80m)	$0.03e^{j56.1^\circ}\begin{bmatrix} 1 & 0.08e^{j-9.5^\circ} \\ 0.33e^{j-52.6^\circ} & 1.23e^{j-163.4^\circ} \end{bmatrix}$

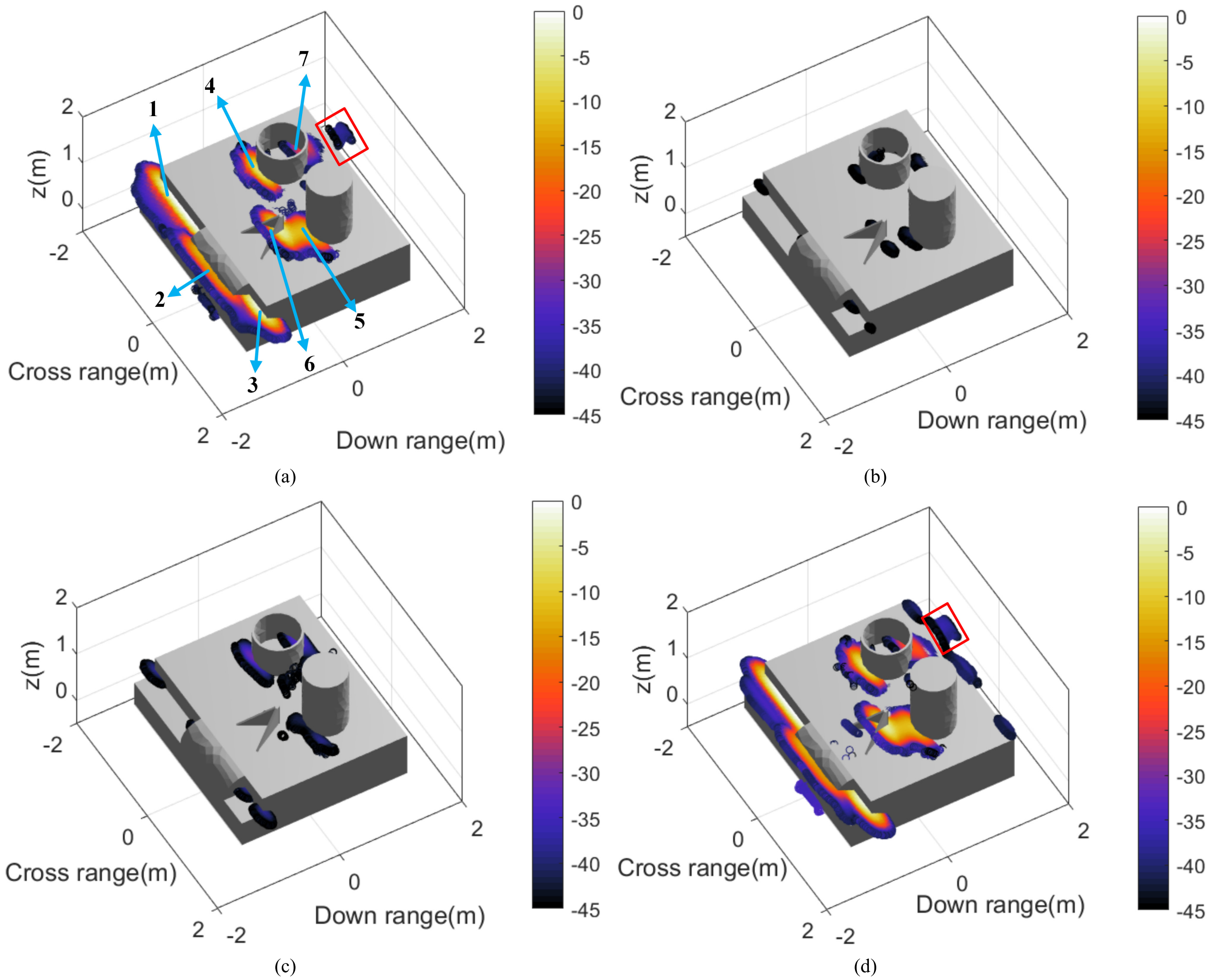

Fig. 4. 3-D high-resolution image of the SLICY model with different polarizations using the proposed technique. (a) HH polarization. (b) HV polarization. (c) VH polarization. (d) VV polarization.

TABLE II
HEIGHT ESTIMATION ERROR OF THE MARKED SCATTERING CENTERS

	Superfast LSE	P-UMUSIC	P-SSD
RMSE(SNR=30dB)	0.009m	0.008m	0.008m
RMSE(SNR=20dB)	0.010m	0.009m	0.009m
RMSE(SNR=10dB)	0.016m	0.011m	0.010m
RMSE(SNR=0dB)	0.043m	0.026m	0.024m

The photograph of the T72 tank from the GTRI dataset is shown in Fig. 5. Measurement parameters of the public dataset are listed in Table III. In addition, the following three facts need to be known when using this public dataset: 1) as can be seen in Fig. 5, there is a complex background environment (e.g., the grassland and forest) around the target area, which means that the received radar echo may contain complex ZDC [41]; 2) the public dataset has a 0.3° periodic data gap in the azimuth dimension, which means that about 0.3° data are missing in every 4.2° azimuth range; and 3) apart from the T72 tank, there are three corner reflectors in the measurement [26], [45]. Two of them were placed on the two sides of the tank, and the third one was placed outside the turntable for calibration purposes.

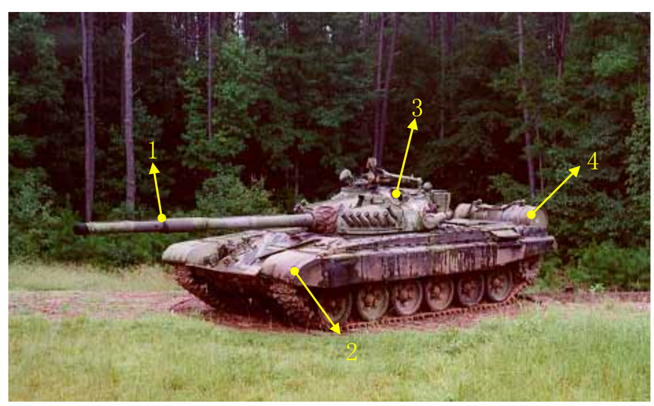

Fig. 5. Photograph of the T72 tank from the GTRI dataset.

Fig. 6(a) shows the 2-D image of the narrow azimuth range (3.03°–6.93°) obtained from the primary baseline. It can be seen that the 2-D image is contaminated by the ZDC, which is inherent to the measurement turntable ISAR imagery. To remove this contamination, we apply the mean sliding

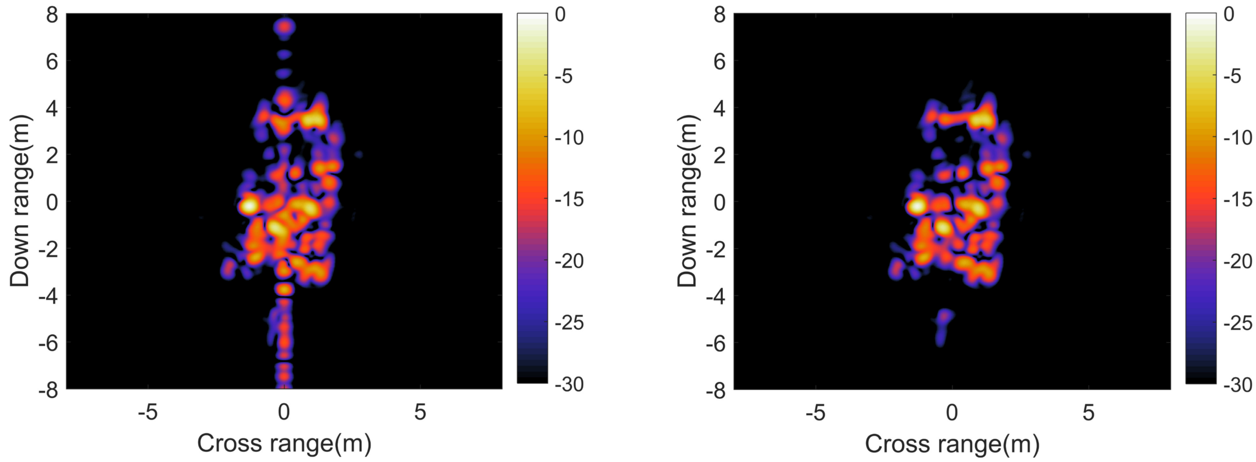

Fig. 6. 2-D image of the primary baseline using narrow azimuth angle (Azimuth range from 3.03°–6.93°, HH polarization). (a) ZDC contaminated 2-D image. (b) ZDC suppressed 2-D image.

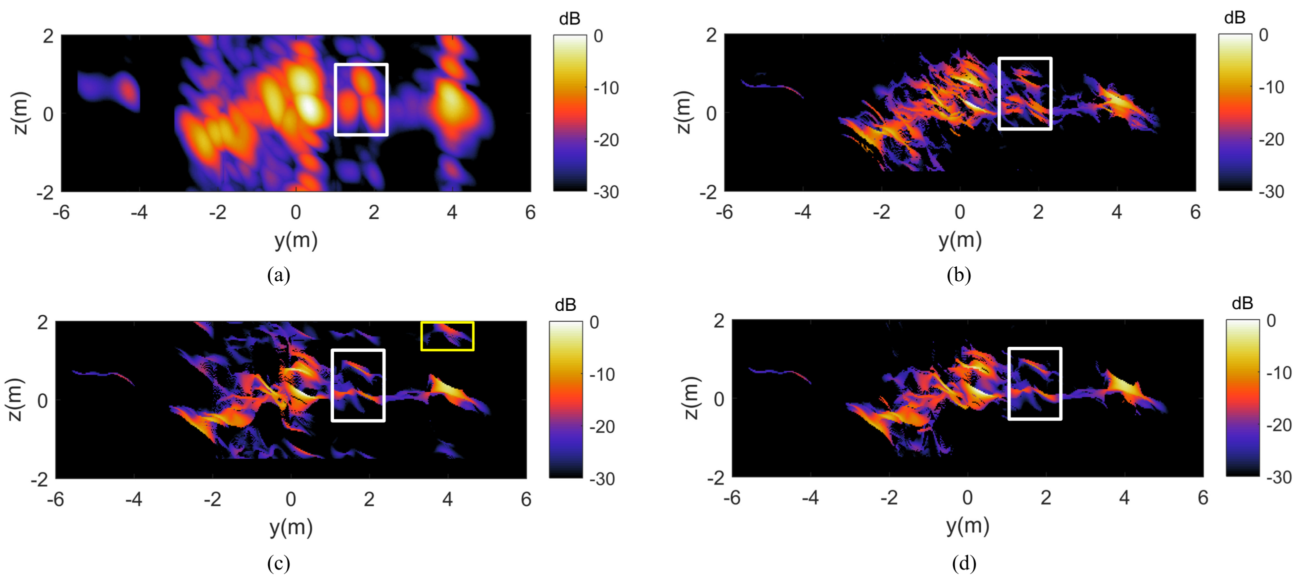

Fig. 7. 2-D projection images of the 3-D reconstruction results using different elevation inversion algorithms (T72 tank, HH polarization). (a) 2-D projection image using FFT. (b) 2-D projection image using Superfast LSE. (c) 2-D projection image using P-UMUSIC. (d) 2-D projection image using P-SSD.

TABLE III
MEASUREMENT PARAMETERS OF THE PUBLIC DATASET

Parameter	Value
Frequency range	9.27GHz-9.93GHz
Frequency step	3MHz
Azimuth angle	0°-360°
Azimuth increment	0.05°
Elevation angle	29.3°-30.7°
Elevation increment	0.14°
Polarization	HH, HV, VH, VV

window [42] to the frequency domain data, and the ZDC suppressed result is displayed in Fig. 6(b).

As shown in Fig. 2(b), the measurement radar path is on a cylindrical surface with a radius of 45.72 m. We use the PEC process described in Section II-A to calibrate the phase error, and then, 11 (baseline) × 4 (polarization) 2-D images are obtained by using G-PFBP to the calibrated data. The imaging plane is chosen to be the slant-range plane, and the strong scattering threshold is set to be $T_{\mathrm{dB}} = 30$. The 2-D projection image using FFT [see Fig. 7(a)] proves that the proposed PEC process could be useful for phase calibration of the measurement data.

Fig. 7(b)–(d) gives 2-D projection results of the down range-elevation plane using different elevation inversion algorithms. As can be seen in the figure, the parameter estimation algorithms perform significant resolution improvement in the elevation direction. As displayed in the marked white box, the scattering points produced by the superfast LSE tend to be more dispersed, whereas the P-UMUSIC and P-SSD give a more compact result. Some sidelobe artifacts are misclassified as the scattering points by the P-UMUSIC (the yellow box). In contrast with the reference algorithms, P-SSD performs more robust in the elevation inversion process.

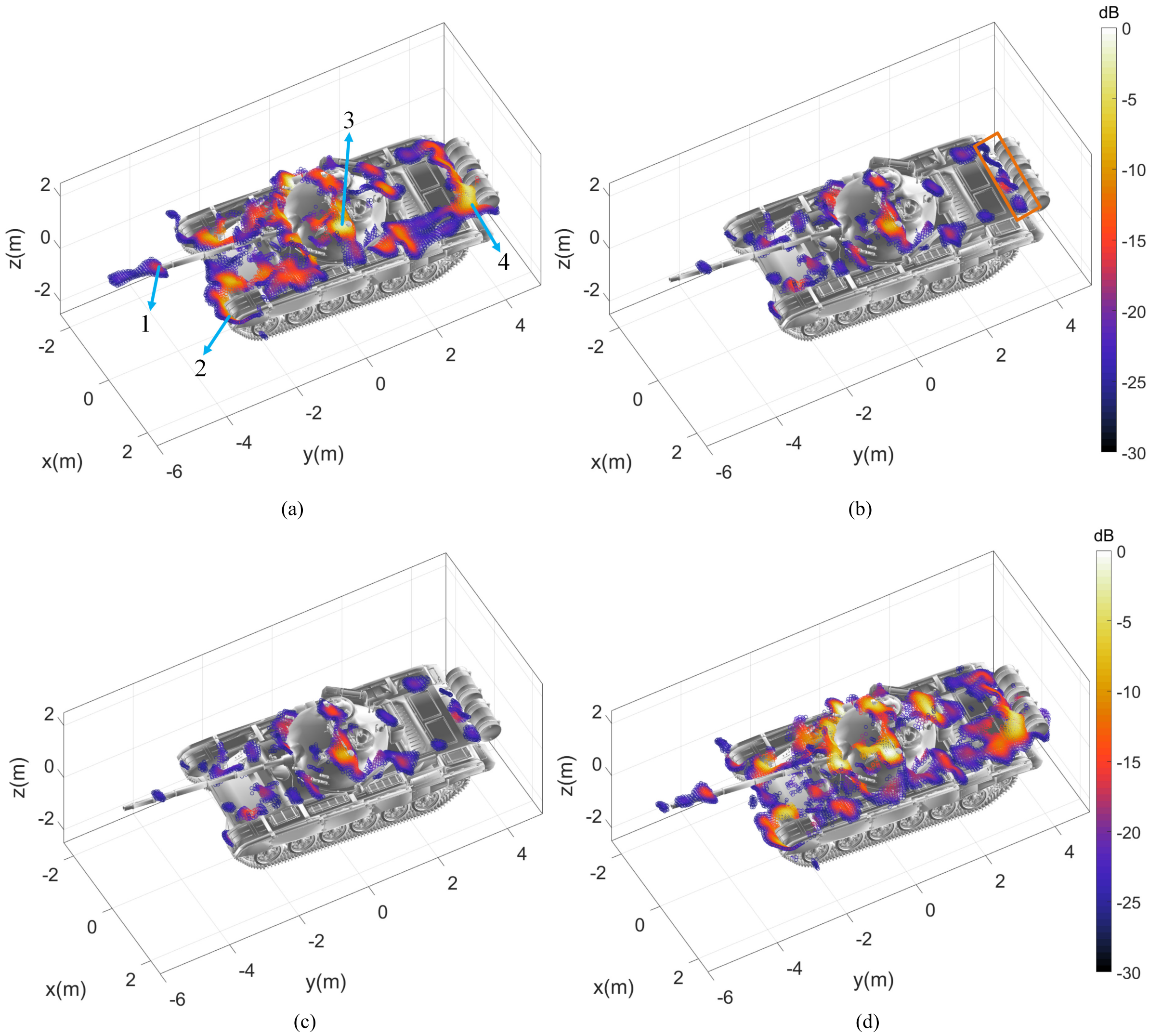

Fig. 8. 3-D high-resolution image of T72 tank with different polarizations using narrow azimuth range data. (a) HH polarization. (b) HV polarization. (c) VH polarization. (d) VV polarization.

Fig. 8 shows the 3-D reconstruction results of the T72 tank using the narrow azimuth range data. The top 30-dB dynamic ranges of each polarization and the corresponding geometry model are displayed. It is noteworthy to point out that the acquired GTRI data have not been processed by the polarization calibration process, and thus, the absolute magnitude of each polarization may not be accurate. As illustrated in this figure, the main backscattering has occurred in the upper surface of the tank, which is consistent with the current coverage of the radar beam. According to the reconstructed scattering features that are matched with the geometry components, we can analyze the scattering mechanism of each scattering center. For instance, there are four marked scattering centers in Fig. 8(a). From the 3-D point cloud in Fig. 8 and the scattering matrix decomposition [5], [41] result in Fig. 9, we can know that the first scattering center is generated by the combined effect of the single- and double-bounces of the gun barrel joint. The second scattering center is produced by the scattering of the track baffle and even-bounce from the track baffle and ground, and the third one is generated by the scattering of the structure composed of the cube and turret. The fourth one is generated by the dihedral-like reflector composed of the plate armor and the oil barrel. In addition, from the HV and VH polarization results in Figs. 8(b) and (c) and 9(c), we can see that the cross-polarization results are relatively weak in the amplitudes, and the scattering mechanisms are different from those in the copolarization results. For example, the diffractions of the edge corner between the plate armor and oil barrel [the orange box in Fig. 8(b)] are clearly visible, whereas the copolarization results focus on all discontinuities between these two components. This scattering characteristic can also be observed in Fig. 4 (scattering centers 1 and 3).

The 3-D reconstruction result (VV polarization) of the T72 tank with full aperture data is presented in Fig. 10. From the multiview of the 3-D reconstruction result, we can see that the outlines of the T72 tank are clearly visible. Strong scatterings are mainly concentrated in the cannon barrel, turret, tracks, oil barrel, and the connection between them. However, due to the accumulation of the measurement error and the periodic data gap, the reconstruction result could not be as

TABLE IV
RUNNING TIME OF THE NUMERICAL DATA AND THE MEASUREMENT DATA

Dataset	Algorithm	Multi-baseline 2-D Imaging (unit/s) $501(x)\times501(y)\times11$(baseline)$\times4$(pol)	Elevation inversion (unit/s)	Total time with G-PFBP (unit/s)
Dataset 1 (SLICY) Data size: $41\times101\times11\times4$	Superfast LSE	2.1 (G-PFBP) / 13.7 (CPU only)	165.4	167.5
	P-UMUSIC		47.7	49.8
	P-SSD		2.8	4.9
Dataset 2 (T-72 sub) Data size: $79\times201\times11\times4$	Superfast LSE	4.6 (G-PFBP) / 30.1 (CPU only)	192.6	197.2
	P-UMUSIC		58.8	63.4
	P-SSD		3.8	8.4
Dataset 3 (T-72 full) Data size: $6721\times201\times11\times4$	Superfast LSE	372.4 (G-PFBP) / 2385.2 (CPU only)	917.3	1289.7
	P-UMUSIC		292.7	665.1
	P-SSD		17.3	389.7

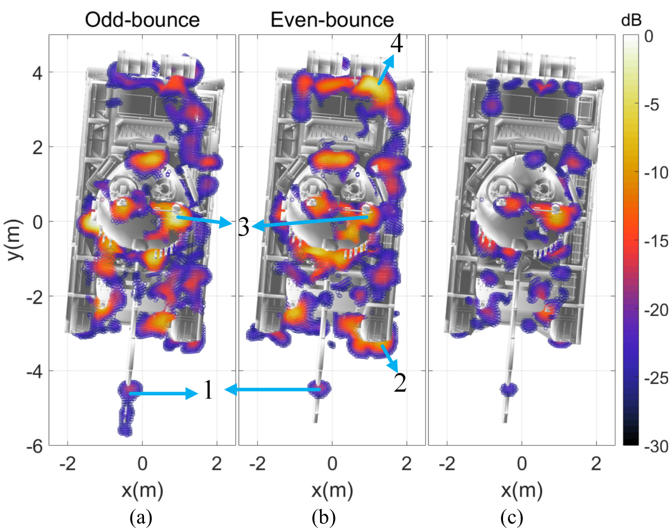

Fig. 9. Scattering matrix decomposition of the 3-D point cloud using the Pauli basis. (a) $\sqrt{2}/2|\mathbf{A}_{\mathrm{HH}}+\mathbf{A}_{\mathrm{VV}}|$. (b) $\sqrt{2}/2|\mathbf{A}_{\mathrm{HH}}-\mathbf{A}_{\mathrm{VV}}|$. (c) $\sqrt{2}/2|\mathbf{A}_{\mathrm{HV}}+\mathbf{A}_{\mathrm{VH}}|$.

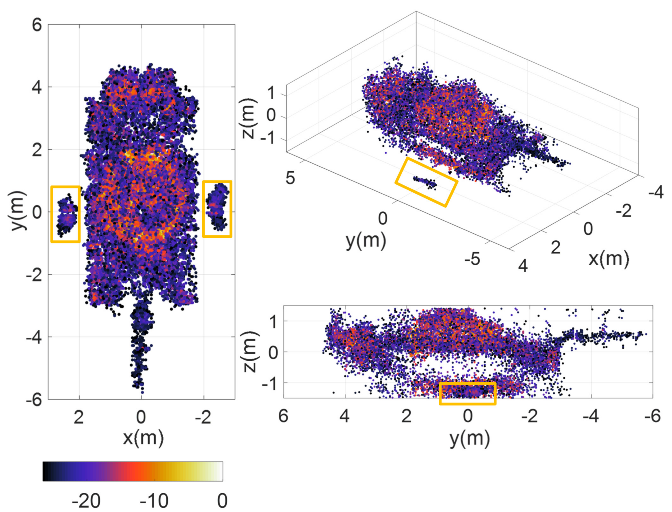

Fig. 10. 3-D reconstruction result of the T72 tank processed by the proposed technique (full aperture data, VV polarization).

smooth as the numerical example. Furthermore, there are two scattering centers located on the two sides of the tank (the yellow box in Fig. 10). According to the locations of these two scattering centers, we can conclude that they are caused by the scattering of the aforementioned corner reflectors [26], [45].

The running time of all data processing is shown in Table IV. All algorithms are implemented in the same

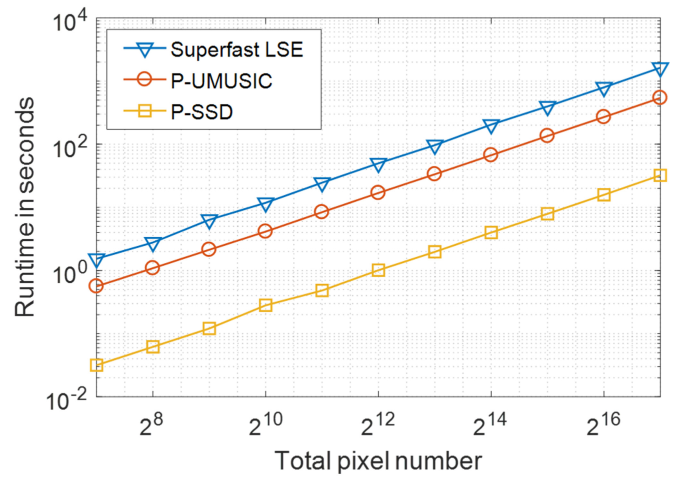

Fig. 11. Running time of the elevation inversion process versus the total pixel number. The baseline number N_φ is set to be 11, and values are averaged over 20 Monte Carlo runs (using the GTRI dataset).

hardware platform: Intel Core i5-9300H 2.40 GHz and NVIDIA GTX 1650. The GTX 1650 has 896 multiprocessors, and the max thread block size is [1024 1024 64]. Notice that all reference algorithms need to use the proposed G-PFBP for multibaseline 2-D imaging, and thus, all the running times of 2-D imaging are the same. Compared to the central processing unit (CPU) only mode, the running time of G-PFBP is reduced by 6.5 times, and the improvement could be further increased when the imaging grid number is increasing. As can be seen in the table, the superfast LSE takes much time in the elevation inversion process since the scattering parameters of each polarization are estimated separately, which means that several processing steps need to be repeated four times. The P-UMUSIC provides a joint estimation, which could save much time for the full polarization data. Nevertheless, the cyclic peak searching process is still considered to be an expensive way for the elevation inversion process because there are thousands of resolution cells to be processed. Without time-consuming peak searching or multiple iteration process, P-SSD uses the matrix decomposition process to obtain the parameters of scattering centers and performs more than ten times faster than the other two algorithms in the elevation inversion process.

In addition, the computational complexity of G-PFBP is $O(N_\varphi N_\theta (N_x N_y)^{5/4})$ [32], where N_θ is the azimuth sample number and N_φ is the baseline number. The computational complexity of P-SSD in elevation inversion is given as $O(h(N_\varphi - L)L^2)$ since the most time-consuming process is the SVD, where h denotes the total pixel number of strong scattering area in a 2-D image and L is the length of the sliding window [see (18)]. The running time scales with the pixel number h are shown in Fig. 11. It can be seen that P-SSD shows stable computational advantages over the other two algorithms. Note that all the results are based on the condition that the baseline number is limited in the practical measurement, whereas some algorithms tend to be more efficient when the baseline number is a large value [39].

V. Conclusion

In this work, a complete ISAR tomography framework is proposed for fully polarimetric 3-D high-resolution imaging. The frequency-domain PEC followed by a GPU accelerated polarimetric filtered backprojection process is developed to obtain the 2-D complex-valued images necessary for 3-D imagery with different baselines and polarization combinations. The 3-D fully polarimetric ISAR images are then reconstructed by extending the SSD to polarimetric signature data. Two examples of real-world complex targets with specific polarimetric scattering mechanisms for both numerical data and outdoor range datasets are processed with high-quality 3-D polarimetric images, demonstrating that the proposed technique is useful for 3-D tomographic reconstruction of outdoor range signature data for real-world complex targets with superior computational efficiency.

References

[1] J. M. L. Sanchez and J. F. Guasch, "3-D radar imaging using range migration techniques," *IEEE Trans. Antennas Propag.*, vol. 48, no. 5, pp. 728–735, May 2000.

[2] Y. Alvarez, Y. Rodriguez-Vaqueiro, B. Gonzalez-Valdes, C. Rappaport, F. Las-Heras, and J. Martinez-Lorenzo, "Three-dimensional compressed sensing-based millimeter-wave imaging," *IEEE Trans. Antennas Propag.*, vol. 63, no. 12, pp. 5868–5873, Dec. 2015.

[3] C. D. Austin, E. Ertin, and R. L. Moses, "Sparse signal methods for 3-D radar imaging," *IEEE J. Sel. Topics Signal Process.*, vol. 5, no. 3, pp. 408–423, Jun. 2011.

[4] K. Ren and R. J. Burkholder, "A 3-D novel fast back-projection imaging algorithm for stratified media based on near-field monostatic and bistatic SAR," *IEEE Trans. Antennas Propag.*, vol. 69, no. 4, pp. 2326–2335, Apr. 2021.

[5] X. Y. Wang, T. Dallmann, R. Moch, and D. Heberling, "ISAR tomography for full-polarimetric 3-D radar cross-section measurements," *IEEE Trans. Antennas Propag.*, vol. 67, no. 4, pp. 2853–2858, Apr. 2019.

[6] D.-J. Yun, J.-I. Lee, K.-U. Bae, J.-H. Yoo, K.-I. Kwon, and N.-H. Myung, "Improvement in computation time of 3-D scattering center extraction using the shooting and bouncing ray technique," *IEEE Trans. Antennas Propag.*, vol. 65, no. 8, pp. 4191–4199, Aug. 2017.

[7] S.-Q. Xing, Y.-Z. Li, D.-H. Dai, and X.-S. Wang, "Three-dimensional reconstruction of man-made objects using polarimetric tomographic SAR," *IEEE Trans. Geosci. Remote Sens.*, vol. 51, no. 6, pp. 3694–3705, Jun. 2013.

[8] X. Xu and R. M. Narayanan, "Three-dimensional interferometric ISAR imaging for target scattering diagnosis and modeling," *IEEE Trans. Image Process.*, vol. 10, no. 7, pp. 1094–1102, Jul. 2001.

[9] O. Ponce, P. Prats-Iraola, R. Scheiber, A. Reigber, and A. Moreira, "First airborne demonstration of holographic SAR tomography with fully polarimetric multicircular acquisitions at L-band," *IEEE Trans. Geosci. Remote Sens.*, vol. 54, no. 10, pp. 6170–6196, Oct. 2016.

[10] A. Budillon, A. Evangelista, and G. Schirinzi, "Three-dimensional SAR focusing from multipass signals using compressive sampling," *IEEE Trans. Geosci. Remote Sens.*, vol. 49, no. 1, pp. 488–499, Jan. 2011.

[11] X. X. Zhu and R. Bamler, "Superresolving SAR tomography for multidimensional imaging of urban areas: Compressive sensing-based TomoSAR inversion," *IEEE Signal Process. Mag.*, vol. 31, no. 4, pp. 51–58, Jul. 2014.

[12] C. D. Austin, E. Ertin, and R. L. Moses, "Sparse multipass 3D SAR imaging: Applications to the GOTCHA data set," *Proc. SPIE*, vol. 7337, Apr. 2009, Art. no. 733703.

[13] G. Fornaro, F. Lombardini, A. Pauciullo, D. Reale, and F. Viviani, "Tomographic processing of interferometric SAR data: Developments, applications, and future research perspectives," *IEEE Signal Process. Mag.*, vol. 31, no. 4, pp. 41–50, Jul. 2014.

[14] F. Gini and F. Lombardini, "Multilook APES for multibaseline SAR interferometry," *IEEE Trans. Signal Process.*, vol. 50, no. 7, pp. 1800–1803, Jul. 2002.

[15] F. Gini, F. Lombardini, and M. Montanari, "Layover solution in multibaseline SAR interferometry," *IEEE Trans. Aerosp. Electron. Syst.*, vol. 38, no. 4, pp. 1344–1356, Oct. 2002.

[16] H. Aghababaee, G. Ferraioli, G. Schirinzi, and V. Pascazio, "Regularization of SAR tomography for 3-D height reconstruction in urban areas," *IEEE J. Sel. Topics Appl. Earth Observ. Remote Sens.*, vol. 12, no. 2, pp. 648–659, Feb. 2019.

[17] D. Xiang, T. Tang, Y. Ban, and Y. Su, "Man-made target detection from polarimetric SAR data via nonstationarity and asymmetry," *IEEE J. Sel. Topics Appl. Earth Observ. Remote Sens.*, vol. 9, no. 4, pp. 1459–1469, Apr. 2016.

[18] Y. Shi, X. X. Zhu, and R. Bamler, "Nonlocal compressive sensing-based SAR tomography," *IEEE Trans. Geosci. Remote Sens.*, vol. 57, no. 5, pp. 3015–3024, May 2019.

[19] L. Kong and X. Xu, "A MIMO-SAR tomography algorithm based on fully-polarimetric data," *Sensors*, vol. 19, no. 22, p. 4839, Nov. 2019.

[20] F. Wang, F. Xu, and Y.-Q. Jin, "Three-dimensional reconstruction from a multiview sequence of sparse ISAR imaging of a space target," *IEEE Trans. Geosci. Remote Sens.*, vol. 56, no. 2, pp. 611–620, Feb. 2018.

[21] P. Prats and J. J. Mallorqui, "Estimation of azimuth phase undulations with multisquint processing in airborne interferometric SAR images," *IEEE Trans. Geosci. Remote Sens.*, vol. 41, no. 6, pp. 1530–1533, Jun. 2003.

[22] S. Tebaldini and A. M. Guarnieri, "On the role of phase stability in SAR multibaseline applications," *IEEE Trans. Geosci. Remote Sens.*, vol. 48, no. 7, pp. 2953–2966, Jul. 2010.

[23] O. Ponce *et al.*, "Fully polarimetric high-resolution 3-D imaging with circular SAR at L-band," *IEEE Trans. Geosci. Remote Sens.*, vol. 52, no. 6, pp. 3074–3090, Jun. 2014.

[24] G. O. Glentis, K. Zhao, A. Jakobsson, and J. Li, "Non-parametric high-resolution SAR imaging," *IEEE Trans. Signal Process.*, vol. 61, no. 7, pp. 1614–1624, Apr. 2013.

[25] U.S. Air Force, Sensor Data Management System. (1997). *GTRI Dataset*. [Online]. Available: https://www.sdms.afrl.af.mil/

[26] M. L. Bryant, L. L. Gostin, and M. Soumekh, "3-D E-CSAR imaging of a T-72 tank and synthesis of its SAR reconstructions," *IEEE Trans. Aerosp. Electron. Syst.*, vol. 39, no. 1, pp. 211–227, Jan. 2003.

[27] Y. He, S.-Y. He, Y.-H. Zhang, G.-J. Wen, D.-F. Yu, and G.-Q. Zhu, "A forward approach to establish parametric scattering center models for known complex radar targets applied to SAR ATR," *IEEE Trans. Antennas Propag.*, vol. 62, no. 12, pp. 6192–6205, 2014.

[28] L. C. Potter and R. L. Moses, "Attributed scattering centers for SAR ATR," *IEEE Trans. Image Process.*, vol. 6, no. 1, pp. 79–91, Jan. 1997.

[29] B. Ding and G. Wen, "Target reconstruction based on 3-D scattering center model for robust SAR ATR," *IEEE Trans. Geosci. Remote Sens.*, vol. 56, no. 7, pp. 3772–3785, Jul. 2018.

[30] W. Doerry, "Basics of polar-format algorithm for processing synthetic aperture radar images," Sandia Nat. Lab., Albuquerque, NM, USA, Tech. Rep. SAND2012-3369, May 2012.

[31] R. L. Moses and L. C. Potter, "Noncoherent 2D and 3D SAR reconstruction from wide-angle measurements," in *Proc. 13th Annu. Adapt. Sens. Array Process. Workshop*. Lexington, MA, USA: MIT Lincoln Lab., 2005, pp. 1–6.

[32] L. A. Gorham and L. J. Moore, "SAR image formation toolbox for MATLAB," *Proc. SPIE*, vol. 7699, Apr. 2010, Art. no. 769906.

[33] K. Naishadham and J. E. Piou, "A robust state space model for the characterization of extended returns in radar target signatures," *IEEE Trans. Antennas Propag.*, vol. 56, no. 6, pp. 1742–1751, Jun. 2008.

[34] L. Ren *et al.*, "Short-time state-space method for micro-Doppler identification of walking subject using UWB impulse Doppler radar," *IEEE Trans. Microw. Theory Techn.*, vol. 66, no. 7, pp. 3521–3534, Jul. 2018.

[35] J.-Y. Lee and L. Greengard, "The type 3 nonuniform FFT and its applications," *J. Comput. Phys.*, vol. 206, no. 1, pp. 1–5, Jun. 2005.

[36] J. P. Burg, "Maximum entropy spectral analysis," Ph.D. dissertation, Dept. Geophys., Stanford Univ., Stanford, CA, USA, 1975.

[37] Z. He, A. Cichocki, S. Xie, and K. Choi, "Detecting the number of clusters in N-way probabilistic clustering," *IEEE Trans. Pattern Anal. Mach. Intell.*, vol. 32, no. 11, pp. 2006–2021, Nov. 2010.

[38] K. Wu and X. Xu, "Two-dimensional augmented state–space approach with applications to sparse representation of radar signatures," *Sensors*, vol. 19, no. 21, p. 4631, Oct. 2019.

[39] T. L. Hansen, B. H. Fleury, and B. D. Rao, "Superfast line spectral estimation," *IEEE Trans. Signal Process.*, vol. 66, no. 10, pp. 2511–2526, May 2018. [Online]. Available: https://github.com/thomaslundgaard/superfast-lse

[40] T. Dallmann and D. Heberling, "Discrimination of scattering mechanisms via polarimetric RCS imaging [measurements corner]," *IEEE Antennas Propag. Mag.*, vol. 56, no. 3, pp. 154–165, Jun. 2014.

[41] S. R. Cloude, "Target decomposition theorems in radar scattering," *Electron. Lett.*, vol. 21, no. 1, pp. 22–24, Jan. 1985.

[42] L. Liang and X. Xu, "Background extraction based on a new calibrator in radar cross section measurements," in *Proc. 12th Int. Conf. Signal Process. Commun. Syst. (ICSPCS)*, Dec. 2018, pp. 1–4.

[43] R. Carriere and R. L. Moses, "High resolution radar target modeling using a modified Prony estimator," *IEEE Trans. Antennas Propag.*, vol. 40, no. 1, pp. 13–18, Jan. 1992.

[44] X. Xu and R. M. Narayanan, "Enhanced resolution in SAR/ISAR imaging using iterative sidelobe apodization," *IEEE Trans. Image Process.*, vol. 14, no. 4, pp. 537–547, Apr. 2005.

[45] M. Soumekh, *Synthetic Aperture Radar Signal Processing With MATLAB Algorithms*. New York, NY, USA: Wiley, 1999.

Kejiang Wu was born in Hunan, China, in 1990. He received the B.S. and M.S. degrees from Beihang University, Beijing, China, in 2014 and 2017, respectively, where he is pursuing the Ph.D. degree.

His research interests include advanced methods on SAR/ISAR imagery and sparse representation of radar signatures.

Xiaojian Xu was born in Jiangxi, China, in 1963. He received the B.S. degree from the Hefei University of Technology, Hefei, China, in 1983, the M.S. degree from the Beijing Institute of Environmental Features (BIEF), Beijing, China, in 1986, and the Ph.D. degree from the University of Nebraska–Lincoln, Lincoln, NE, USA, in 2002, all in electrical engineering.

From 1986 to 1999, he was with BIEF, where he was mainly involved in research of electromagnetic scattering modeling and microwave imaging. From June 1999 to December 2002, he was with the Environmental Remote Sensing Laboratory, University of Nebraska–Lincoln, where his research work was on ultrawideband random noise radar with emphasis on foliage and ground-penetration applications. Since January 2003, he has been with the School of Electronic and Information Engineering, Beihang University, Beijing, as a Signal and Information Processing Professor. His research interests include remote sensing signatures, radar imagery, target recognition, and system modeling.